# Unlocking the Potential of Li-Ag Alloys: Phase Selection and Practical Application

Yuping Huang [a,b], Shiwei Chen [a,b], Yu Yang [a], Zhe-Tao Sun [a,b], Xinyu Yu [a,b], Chaohong Guan [a], Runxin Ouyang [a], Yunlong Guo [a], Shou-Hang Bo [b,c,*], Hong Zhu[a,*]

[a] University of Michigan–Shanghai Jiao Tong University Joint Institute, Shanghai Jiao Tong University, 800, Dongchuan Road, Shanghai 200240, China

[b] Future Battery Research Center, Global Institute of Future Technology, Shanghai Jiao Tong University, Shanghai 200240, China

[c] School of Chemistry and Chemical Engineering, Shanghai Jiao Tong University, Shanghai 200240, China

Corresponding Author *E-mail: shouhang.bo@sjtu.edu.cn, hong.zhu@sjtu.edu.cn.

## Abstract

Dendrite formation, contact loss, and continuous formation of the solid electrolyte interphase (SEI) preclude the practical use of the energy-dense lithium (Li) metal. Li-Ag alloys have the potential to address these issues due to their exceptional lithiophilicity, outstanding mechanical stability, and moderate chemical stability. This study evaluates all phases in the Li-Ag phase diagram based on lithiation capacity, Li insertion, mechanical property, and chemical stability. Our findings suggest that $Li_4Ag$ is the most promising phase, and the Gibbs free energy of nucleation ($\Delta G_{\mathrm{nucle}}$) for Li-Ag alloys is 3 to 5 orders of magnitude smaller compared to pure Li, resulting in uniform nucleation and deposition behavior. We proposed practical applications within the $Li_4Ag$ phases or from the $Li_9Ag_4$ to the $Li_4Ag$ phases, which may provide a usable capacity of 409 to 696 mAh/g, respectively. Experiments indicate that $Li_4Ag$ exhibits not only the smallest impedance but also the highest capacity retention compared to $Li_9Ag_4$ and pure Li. The study provides valuable guidance for the selection and application of Li-containing alloys in future battery development.

**Keywords:** Li-Ag alloys, phase selection, practical application

# Introduction

All-solid-state Li batteries (ASSLBs) have gained significant attention for their potential to achieve high energy density at the cell level, surpassing 400 Wh/kg, making them crucial for applications in electric vehicles and portable electronics.[1–5] This is primarily attributed to the exceptional properties of the Li metal anode (LMA), which include its high gravimetric capacity (3860 mAh/g) and the lowest electrochemical potential (−3.04 V versus the standard hydrogen electrode).[6–8] However, the LMA itself faces inherent challenges as an electrode material, primarily due to three reasons: (1) High chemical reactivity:[9–12] The side reactions between the LMA and the solid-state electrolyte are intricate, leading to the continuous formation of the SEI. These reactions also contribute to a reduction in coulombic efficiency and an increase in the interfacial impedance of the battery. (2) Contact loss:[13–15] During cycling, localized volumetric changes in the LMA result in contact loss with the solid-state electrolyte, undermining the battery's cycle life. (3) Li dendrites:[16–20] Nonuniform deposition of Li can lead to the formation and growth of Li dendrites. These Li dendrites have the potential to penetrate solid-state electrolytes, posing safety hazards.

The integration of silver (Ag) into LMA is a highly effective approach to address the aforementioned three challenges, attributed to its moderate chemical stability to reduce the side reaction and inhibit the continuous formation of the SEI. Furthermore, Li-Ag alloys exhibit exceptional mechanical stability, resulting in enhanced cycling stability during the repetitive processes of Li plating and stripping at the anode.[21] Additionally, Ag and Li-Ag alloys demonstrate remarkable affinity towards Li (lithiophilicity), enabling uniform deposition of Li and suppressing the formation of Li dendrites.[22] Additionally, subtle structural alterations and chemical potential gradients in Li-Ag alloys significantly enhance reversibility in Li-alloying/dealloying processes, contributing to improved cycling stability. [23] For instance, Li et al. developed Li-alloy leaves with excellent mechanical properties by adding 1 at% Ag into Li, making them suitable for mass production.[24] Liu et al. developed a dual protection layer consisting of $Li_3Ag$ and $Li_{0.98}Ag_{0.02}$, which effectively inhibits Li dendritic growth and enhances the safety of the battery.[25] Although Li-Ag alloys are studied as substitutes for LMA, the question remains as to which specific Li-Ag alloy phase should be chosen from the different phase regions in the complex Li-Ag phase diagram, as well as which composition range should be used for charging and discharging to achieve the best performance in practical applications.

The chemical stability, mechanical properties, and Li insertion influence the electrochemical performance of batteries.[26–30] The chemical stability of the anode in the battery refers to its ability to resist unwanted chemical reactions or corrosion. The process of extracting Li from the electrolyte and inserting it into the anode is known as Li insertion. The mechanical property of alloy anodes relates to their ability to resist external forces without damage. On the other hand, the capacity of alloy anode impacts its energy density, and alloy anodes with a capacity greater than that of graphite (372 mAh/g) are likely to have practical applications.

In this study, we employed density functional theory (DFT) calculations to explore the chemical stability, Li insertion, mechanical property, and capacity characteristics of various phases in the Li-Ag phase diagram. Our findings indicate that $Li_4Ag$ exhibits the best performance in terms of the factors above, followed by $Li_9Ag_4$. Subsequently, we performed tests on nucleation overpotential ($\eta$), Electrochemical Impedance Spectroscopy (EIS), voltage stability, and cycling performance, aligning with the findings from DFT calculations. Herein, we recommend the practical application within the $Li_4Ag$ or from the $Li_9Ag_4$ phase to the $Li_4Ag$ phase for Li-Ag alloys. Overall, this work offers guidance for selecting high-performance phases in other alloy solid solutions.

## Computational methodology

All calculations utilized the projector augmented wave (PAW)[31] method within the framework of density functional theory (DFT) as implemented in the Vienna Ab-initio Simulation Package (VASP).[32] The exchange functional chosen was the Perdew-Burke-Ernzerhof (PBE),[33] which falls under the generalized gradient approximation (GGA). The cutoff energy for the plane wave was set to 520 eV, and the Brillouin zone integration utilized a Gamma-centered grid with a 2 × 2 × 2 *k*-point mesh. The convergence criteria for energy and force were set at $10^{-5}$ eV/atom and 0.01 eV/Å, respectively.

The surface energy ($\gamma$) quantifies the energy difference between a surface slab structure and the bulk structure:[34]

$$\gamma = \frac{E_{\mathrm{slab}} - E_{\mathrm{bulk}}}{2A} \tag{1}$$

where $E_{\mathrm{slab}}$ represents the total energy of the slab structure, $E_{\mathrm{bulk}}$ represents the total energy of the bulk structure, and $A$ represents the surface area. To investigate the surface energy of the six Li-Ag phases, 2×2×2 supercell models with a 12 Å vacuum layer along the $Z$ direction were employed to prevent interactions between repeated slabs for symmetric (100), (110), and (111) slab models with different terminations. For more information on the surface models, please refer to Table S1 in the Supporting Information.

For adsorption energy calculations, a Li atom was placed at a distance of 3 Å from the surface. Three different adsorption sites were considered: bridge, hollow, and top. The adsorption energy of a Li atom was calculated using the following equation:[30]

$$E_{\mathrm{ads}} = E_{\mathrm{slab+Li}} - E_{\mathrm{slab}} - E_{\mathrm{Li}} \tag{2}$$

Here, $E_{\mathrm{slab+Li}}$ represents the total energy of the system with the Li atom bound to the surface, $E_{\mathrm{slab}}$ is the energy of the slab without the Li adatom, and $E_{\mathrm{Li}}$ is the energy per Li atom in the bulk BCC lithium phase.

The energy barriers for Li-ion migration were calculated using the climbing image nudged elastic band (CI-NEB) method[35] in the supercell model with a single Li vacancy. This method allows for determining the energy landscape and identifying transition states along the migration pathway of Li ions.

## Experimental methodology

All cells were assembled in an Ar-filled glove box with oxygen and water content below 0.01 parts per million (ppm). The molds used to create the solid-state cells were explicitly designed and consisted of two stainless steel bars and a cylinder made of poly(etherether-ketone) (PEEK) with a 10 mm internal diameter. $Li_6PS_5Cl$ (LPSC) and

$Li_3InCl_6$ (LIC) were purchased from MTI Corporation, China, and $LiNbO_3$-coated $LiNi_{0.8}Co_{0.1}Mn_{0.1}O_2$ (LNO@NCM811) was obtained from CN New Energy, China.

We assembled $Li_4Ag$|LPSC|$Li_4Ag$, $Li_9Ag_4$|LPSC|$Li_9Ag_4$ and Li|LPSC|Li symmetric cells. For $Li_4Ag$|LPSC|$Li_4Ag$, 120 mg of LPSC powder was initially placed into the mold and pre-pressed at 50 MPa for 1 minute. Subsequently, two Ag foils (8.2 mg each) were affixed to both sides of the LPSC pellet, and the entire cell was pressed at 370 MPa for 10 minutes. Then, two Li foils (2.1 mg each, molar ratio of Li:Ag ≈ 4:1) were pressed onto the two Ag foils, and the cell was compressed at 100 MPa and rested for 6 hours. Due to the interdiffusion between Li and Ag, spontaneous alloying occurred, forming $Li_4Ag$. The assembly process for the $Li_9Ag_4$|LPSC|$Li_9Ag_4$ cell remained the same, with the only difference being the electrode configuration, where 1.2 mg Li foils were used. For the Li|LPSC|Li cell, after pelleting the LPSC, two Li foils were attached to both sides, and the cell was pressed at 10 MPa.

In addition, we also assembled Li|LPSC|$Li_4Ag$ and Li|LPSC|$Li_9Ag_4$ half cells. For the Li|LPSC|$Li_4Ag$ cell, the assembly process began with adding 120 mg of LPSC powder to the mold, followed by pre-pressing at 50 MPa for 1 minute. Subsequently, an Ag foil was affixed to one side of the LPSC pellet, and the entire cell was pressed at 370 MPa for 10 minutes. Next, a Li foil was pressed onto the Ag foil, and the cell was further pressed at 100 MPa and rested for 6 hours. Afterward, a Li foil was attached to the other side of the LPSC pellet, and the cell was pressed at 10 MPa. The Li|LPSC|$Li_9Ag_4$ cell was assembled using the same method except for the electrode change.

Finally, we assembled $Li_4Ag$|LPSC|LNO@NCM811, $Li_9Ag_4$|LPSC|LNO@NCM811, and Li|LPSC|LNO@NCM811 full cells. For the full cell, such as $Li_4Ag$|LPSC|LNO@NCM811, we added 80 mg of LPSC powder to the mold, which was then pre-pressed at 50 MPa for 1 minute. Subsequently, we evenly distributed 40 mg of LIC powder and 10 mg of a composite cathode material (consisting of LNO@NCM811, LIC, and CNT with a mass ratio of 60:40:4) on one side of the LPSC pellet in sequence. An Ag foil was attached to the opposite side of the LPSC pellet. The entire cell was then pressed at 370 MPa for 10 minutes. Following that, a Li foil was pressed onto the Ag foil, and the cell was pressed at 100 MPa and rested for 6 hours. The $Li_9Ag_4$|LPSC|LNO@NCM811 cell was assembled using the same method, with the only difference being the change in the anode. The Li|LPSC|LNO@NCM811 cell was similarly prepared, but its stacking pressure was set to 10 MPa.

Solid-state cell molds have seals to keep air out, so all electrochemical testing was conducted outside the glove box. The galvanostatic charge/discharge tests were also performed at 25℃ under 100 MPa and 10 MPa for the cells using Li-Ag alloy and Li metal as the anodes, respectively. A NETWARE CT-4000 battery test system was used in the galvanostatic tests. Electrochemical impedance spectroscopy (EIS) was performed using a Biologic SP-200 from 7 MHz to 0.1 Hz with an AC amplitude of 10 mV.

## Results and Discussion

### Voltage, volume expansion, stability calculation

Ag displays a notable attribute through the formation of multiple different phases with Li. With increasing Li concentration, six single solid phase regions will emerge, namely Ag, LiAg, $Li_9Ag_4$, $Li_4Ag$, $Li_9Ag$, and Li, corresponding to the $\alpha$ phase, $\beta$ phase, $\gamma_3$ phase, $\gamma_2$ phase, $\gamma_1$ phase, and $\delta$ phase,[36–38] respectively. Details are shown in Figure S1.

High output voltage is critical in achieving high energy density in ASSLBs. Theoretical voltage (as defined in equation S2) of Li-Ag alloys were calculated to be 0.342, 0.230, 0.121, 0.091, 0.030, and 0 V for the Ag, LiAg, $Li_9Ag_4$, $Li_4Ag$, $Li_9Ag$ and Li, respectively, as shown in Figure 1a. These results agree well with previous findings.[36,39] Interestingly, the average voltage of Li-Ag alloys (0.175 V) is lower compared to other Li-containing alloys[40–42] such as Li-In (0.3 V), Li-Sn (0.504 V), Li-Sb (0.948 V), Li-Al (0.3 V), and Li-Si (0.4 V). This suggests that Li-Ag alloys hold promise as anode materials for ASSLBs.

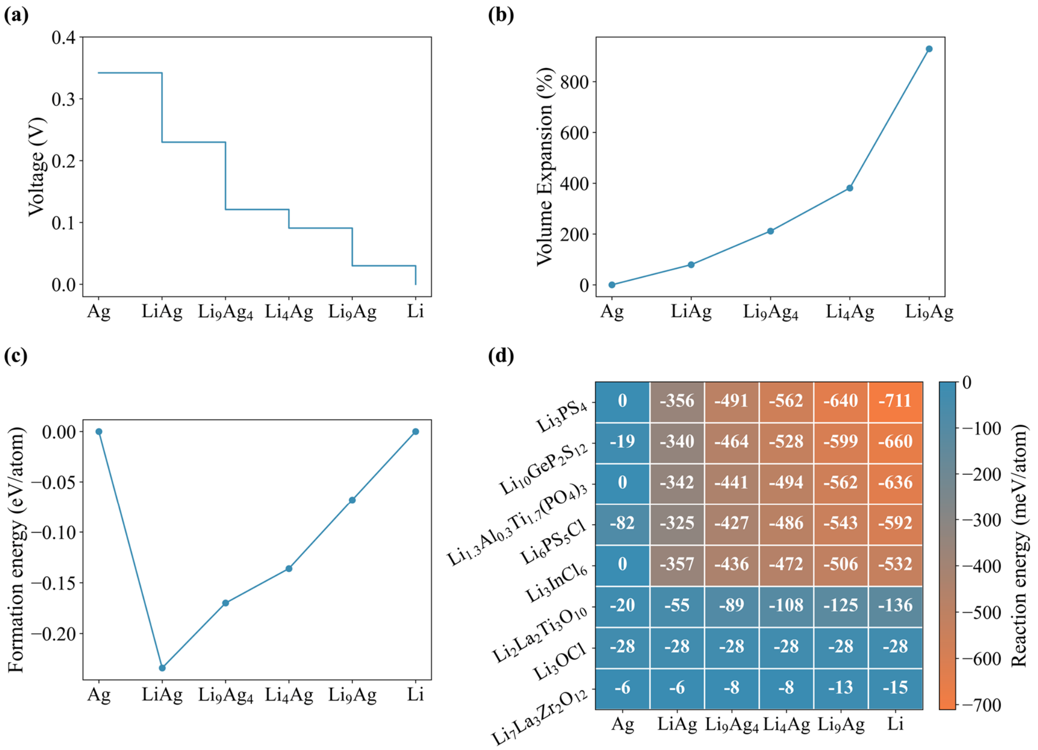

Figure 1. Calculated Li-Ag alloys' basic properties: (a) Voltage platform of various Li-Ag phases. (b) Volume expansion. (c) Formation energy of six different Li-Ag phases. (d) Reaction energy between Li-Ag alloys and eight solid-state electrolytes.

Small volume expansion during Li insertion/extraction is important in maintaining favorable cycling stability. We conducted DFT calculations, as defined in equation S4, to determine the volume expansions of various Li-Ag alloys, as illustrated in Figure 1b. The volume expansions of Ag, LiAg, $Li_9Ag_4$, $Li_4Ag$, and $Li_9Ag$ are calculated to be 0%, 79.4%, 211.6%, 381.2%, and 929.1%, respectively, consistent with previous literature.[36,39]

We evaluate the thermodynamic stability of the Li-Ag alloys based on the formation energy, as defined in equation S3. As depicted in Figure 1c, the six phases considered are thermodynamically stable. The heat map in Figure 1d illustrates the calculated reaction energy between Li-Ag alloys and eight solid-state electrolytes: $Li_5PSCl_6$, $Li_7La_3Zr_2O_{12}$, $Li_{10}GeP_2S_{12}$, $Li_{1.3}Al_{0.3}Ti_{1.7}(PO_4)_3$, $Li_2La_2Ti_3O_{10}$, $Li_3OCl$, $Li_3PS_4$, and $Li_3InCl_6$. It shows that the Li-Ag alloys exhibit relatively low reaction energy (–15 to –

6 meV/atom) against $Li_7La_3Zr_2O_{12}$, indicating that $Li_7La_3Zr_2O_{12}$ is the most suitable solid-state electrolyte for the studied systems. $Li_3PS_4$ is the least compatible with Li-Ag alloys. Our results agree well with previous experimental findings.[43] Besides, as the Li concentration increases in Li-Ag alloys, the interfacial reaction energy becomes more negative, indicating higher reactivity between the anode and the electrolyte.

## Li insertion

We assume Li insertion as a multi-step process that involves three essential stages[30]: Li adsorption, nucleation, and diffusion (Figure 2a). These steps are all crucial for the operation of ASSLBs and greatly influence the overall performance of the cell.

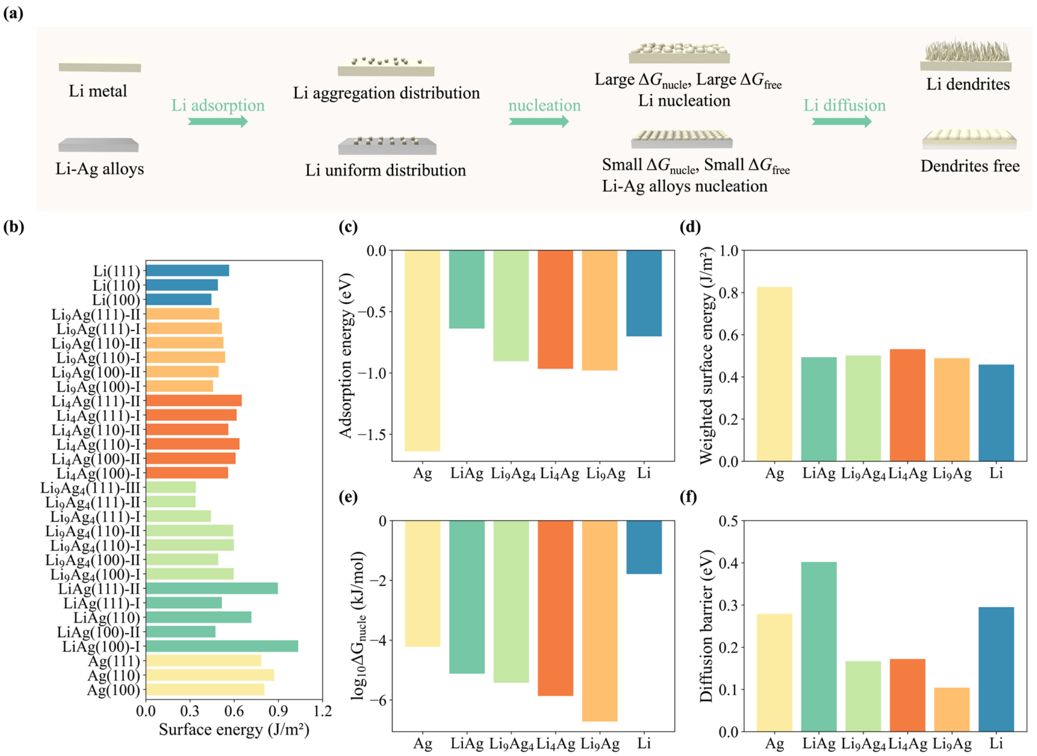

Figure 2. The process of Li insertion. Li-Ag alloys have better Li insertion capability than pure Li. (a) Schematic diagram of adsorption, nucleation, and diffusion processes of Li metal and Li-Ag alloys, (b) Surface energy, (c) Li adsorption energy, (d) Weighted surface energy, (e) Gibbs free energy of nucleation, and (f) Li diffusion barrier of Li-Ag phases.

Surface energy refers to the amount of energy required to create a unit area of a new surface during nucleation and growth of Li atoms on the surface of an alloy. According to Figure 2b, the most stable surfaces for Ag, LiAg, $Li_9Ag_4$, $Li_4Ag$, $Li_9Ag$, and Li are

(111), (100), (111), (100), (100), and (100), respectively. The corresponding surface energy for these surfaces are 0.784, 0.473, 0.338, 0.559, 0.456, and 0.445 J/m$^2$. The most stable surfaces were used in the Li adsorption energy calculations. More detailed information about surface energy and models for Ag, LiAg, $Li_9Ag_4$, $Li_4Ag$, and $Li_9Ag$ can be found in Table S1.

The Li insertion process begins with the crucial step of Li adsorption, and the Li adsorption energy has been extensively studied using DFT calculations. Figure 2c illustrates that the most favorable adsorption site is typically the hollow site. Specific values for the adsorption energy at all sites can be found in Table S2. For Ag, LiAg, $Li_9Ag_4$, $Li_4Ag$, $Li_9Ag$, and Li, the adsorption energies are –1.638, –0.638, –0.905, –0.966, –0.980, and –0.702 eV, respectively. These findings provide compelling evidence that most Li-Ag alloys exhibit lower adsorption energies than pure Li, except for LiAg. Moreover, as the Li concentration in the alloy increases from LiAg to $Li_9Ag$, there is a consistent decrease in the adsorption energy. This trend suggests that Li can be more easily adsorbed onto the substrate as the Li concentration in the alloy increases.

The nucleation process of Li-Ag alloys impacts the stability and safety of battery, making it crucial to understand and control Li-Ag alloys nucleation. The nucleation process of Li-Ag alloys can be understood by using classical equations for nucleation as follow:

$$x\mathrm{Li}^{+} + x\mathrm{e}^{-} + y\mathrm{Ag} = \mathrm{Li}_x\mathrm{Ag}_y \tag{3}$$

$$\Delta G_{\mathrm{free}} \approx \Delta E = E\left(\mathrm{Li}_x\mathrm{Ag}_y\right) - xE(\mathrm{Li}) - yE(\mathrm{Ag}) \tag{4}$$

$$\Delta G_{\mathrm{v}} = \frac{\Delta G_{\mathrm{free}}}{V_{\mathrm{m}}} \tag{5}$$

$$\Delta G_{\mathrm{nucle}} = \left(\frac{16\pi\gamma^3}{3\Delta G_{\mathrm{v}}^{\;2}}\right)\left(\frac{2 - 3\cos\theta + \cos^3\theta}{4}\right) \tag{6}$$

$$\bar{\gamma} = \Sigma\,\gamma f \tag{7}$$

In the above equations, $\Delta G_{\mathrm{nucle}}$ is the Gibbs energy required for the formation of a spherical nucleus with a radius $r$.[44] The free energy ($\Delta G_{\mathrm{free}}$) expressions are often approximated using the differences in total energy between products and reactants,[45] which can be readily obtained through DFT calculations. $\Delta G_{\mathrm{v}}$ represents the free energy change per unit volume, and $\gamma$ represents the surface energy. The variables $V_{\mathrm{m}}$ corresponds to the molar volume of Li in the Li-Ag alloys. $\theta$ refers to the wetting angle between the Li nucleus and the substrate. $\bar{\gamma}$ represents the weighted surface energy, while $f$ represents the fraction of the {hkl} family's area in the Wulff shape, which is depicted in Figure S2.

According to the data shown in Figure 2d, the $\bar{\gamma}$ (calculated by equation (7)) for Ag, LiAg, $Li_9Ag_4$, $Li_4Ag$, $Li_9Ag$, and Li are 0.826, 0.493, 0.501, 0.531, 0.488, and 0.458 $J/m^2$, respectively. It is evident that all Li-Ag alloys possess larger $\bar{\gamma}$ than Li. Previous studies have indicated that a higher surface energy leads to the densification of Li plating rather than whisker growth.[46,47] Therefore, Li-Ag alloys may enhance interfacial stability and cycling performance.

When $\Delta G_{\mathrm{nucle}}$ is small, it requires less energy, making nucleation easier. Hence, calculating $\Delta G_{\mathrm{nucle}}$ is meaningful. To determine $\Delta G_{\mathrm{nucle}}$, we rely on equations (4) to (6). We obtain $\Delta G_{\mathrm{free}}$ through DFT calculations, applied $\gamma$ with the $\bar{\gamma}$ values,[48] and reference $\theta$ data from Wang's previous work.[49] All the relevant data is presented in Table S3. As illustrated in Figure 2e, Li-Ag alloys exhibit significantly smaller $\Delta G_{\mathrm{nucle}}$ compared to pure Li. The $\Delta G_{\mathrm{nucle}}$ for Ag, LiAg, $Li_9Ag_4$, $Li_4Ag$, $Li_9Ag$, and Li are $6.00\times10^{-5}$, $7.57\times10^{-6}$, $3.77\times10^{-6}$, $1.36\times10^{-6}$, $1.89\times10^{-7}$, and $1.63\times10^{-2}$ kJ/mol, respectively. Li-Ag alloys' $\Delta G_{\mathrm{nucle}}$ are smaller by 3 to 5 orders of magnitude compared to pure Li. Since the nucleation overpotential ($\eta$) for Li is measured at 6 mV (Figure 5a), it is expected that Li-Ag alloys should have $\eta$ close to 0, which aligns with the experimental data we obtained (Figure 5a). Our calculations provide a robust explanation for why the $\eta$ of Li-Ag alloys is zero in experimental observations. In summary, Li-Ag alloys exhibit smaller $\Delta G_{\mathrm{free}}$ and $\Delta G_{\mathrm{nucle}}$ compared to pure Li, facilitating easier and more uniform nucleation, thereby enhancing interface stability, safety, and cycling performance.

The final step in Li insertion is the Li diffusion process within the material. As Figure 2d shows, the energy barriers associated with Li diffusion for Ag, LiAg, $Li_9Ag_4$, $Li_4Ag$, $Li_9Ag$, and Li are 0.279, 0.402, 0.167, 0.171, 0.104, and 0.295 eV, respectively. Among the Li-Ag alloy phases considered, $Li_9Ag_4$, $Li_4Ag$, and $Li_9Ag$ have more minor Li diffusion energy barriers compared to pure Li. This indicates that $Li_9Ag_4$, $Li_4Ag$, and $Li_9Ag$ exhibit a better Li transport rate than pure Li.

## Mechanical property

To assess the mechanical stabilities of Li-Ag alloys, we performed calculations to determine the key mechanical properties (Figure 3): Bulk modulus ($B$), Young's modulus ($E$), Shear modulus ($G$), Poisson's ratio ($v$), and the $B/G$ ratio. The $B$ quantifies the volume compression behavior, while $E$ reflects the system's stiffness. $G$ measures the material's elasticity under shear forces.[52] $v$ indicates the expansion of a material when compressed in the transverse direction and can serve as an approximate measure of plastic ductility.[53] The $B/G$ ratio is a significant parameter for assessing the predominant elasticity or plasticity of a crystalline material. Ductile materials generally exhibit a high $B/G$ ratio (above 1.75), suggesting their feasibility for plastic deformation, while brittle materials typically have a low $B/G$ ratio (below 1.75).[54,55] The calculated elastic constants are provided in Table S4, and elastic stability criteria demonstrating that all the mentioned elastic constants meet the Born criteria for mechanical stability[56] at the DFT level (0 K) in Li-Ag alloys (the detailed values can be found in the Table S5).

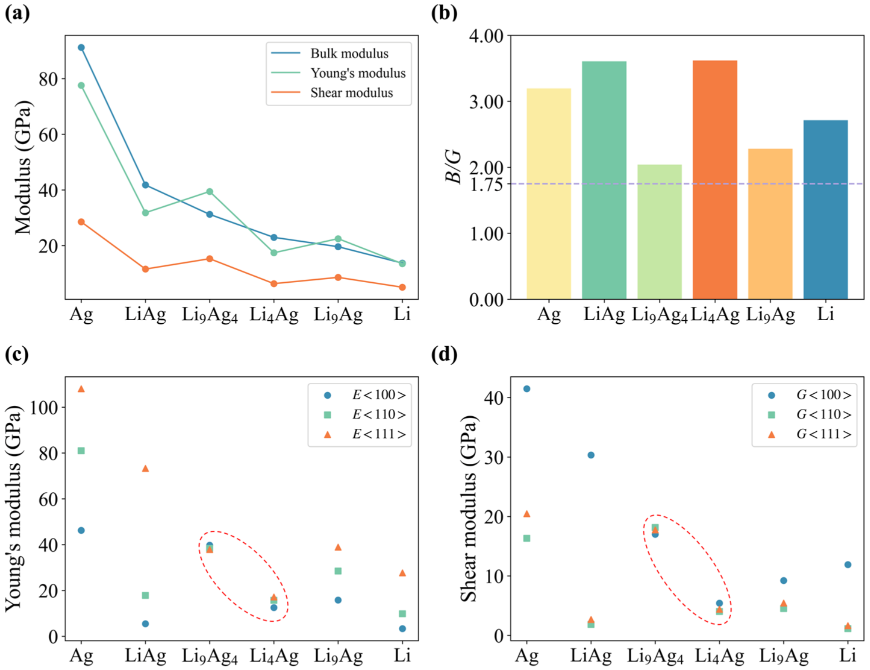

Figure 3. Mechanical property for Li-Ag alloys. (a) Bulk modulus ($B$), Young's modulus ($E$), and shear modulus ($G$). (b) The ratio of $B/G$. (c) Young's modulus for three crystallographic orientations: $E$<100>, $E$<110>, and $E$<111>. (d) Shear modulus for three crystallographic orientations: $G$ <100>, $G$ <110>, $G$ <111>.

In Table 1, we present the elastic properties, and Figure 3a illustrates the variation of these properties with Li concentration. Generally, there is an almost linear decrease in the *B*, *E*, and *G* as the Li concentration increases. This indicates that the structures become more elastic and compressible with higher Li content, which aligns with findings in other Li-containing alloys.[51,52] This trend may be attributed to the formation of more Li-Li bonds as the Li content increases, which diminishes the material's resistance to deformation. Figure 3b depicts the *B*/*G* ratios of Ag, LiAg, $Li_9Ag_4$, $Li_4Ag$, $Li_9Ag$ and Li, which are 3.195, 3.607, 2.090, 3.619, 2.282, and 2.714, respectively, based on our elastic property calculations. The *B*/*G* ratios of the Li-Ag alloys range from 2.090 to 3.619, suggesting that all investigated Li-Ag alloys possess good ductility. Notably, $Li_4Ag$ exhibits the highest ductility among the Li-Ag alloys.

Table 1. Mechanical properties of Li-Ag alloys.

| Phases | *B* (GPa) | *E* (GPa) | *G* (GPa) | *v* | *B*/*G* |
|---|---|---|---|---|---|
| Ag | 91.186 | 77.534 | 28.541 | 0.358 | 3.195 |
| LiAg | 41.782 | 31.806 | 11.582 | 0.373 | 3.607 |
| $Li_9Ag_4$ | 31.218 | 39.451 | 15.298 | 0.289 | 2.090 |
| $Li_4Ag$ | 22.959 | 17.428 | 6.344 | 0.373 | 3.619 |
| $Li_9Ag$ | 19.610 | 22.491 | 8.592 | 0.309 | 2.282 |
| Li | 13.716 | 13.504 | 5.054(~5 ref [50]) | 0.336(~0.33 ref [51]) | 2.714 |

Figures 3c and 3d depict the direction-dependent *E* and *G* for Li-Ag alloys. In Figure 3c, it is evident that the <111> orientation represents the highest level of rigidity, whereas <100> indicates the most compliant direction. Figure 3c reveals that *E* for $Li_9Ag_4$ along <100>, <110>, and <111> are 39.755, 38.350, and 37.903 GPa, respectively. In contrast, $Li_4Ag$ exhibits *E* values of 12.551 GPa for *E*<100>, 15.714 GPa for *E*<110>, and 17.155 GPa for *E*<111>. Comprehensive values for all Li-Ag alloys can be found in Table S6, with the calculation methodology aligning with prior reports.[28,57] In Figure 4d, $Li_9Ag_4$ have *G* of 17.016 GPa for *G*<100>, 18.155 GPa for *G*<110>, and 17.759 GPa for *G*<111>. Likewise, $Li_4Ag$ exhibits an average shear modulus of 5.422 GPa for *G*<100>, 4.023 GPa for *G*<110>, and 4.401 GPa for *G*<111>. In summary, $Li_9Ag_4$ and $Li_4Ag$ exhibit isotropic modulus due to small differences in direction-dependent $E$ or $G$, while the other Li-Ag alloys demonstrate anisotropic modulus. Isotropic modulus leads to isotropic expansion, which is favorable for the electrochemical performance of batteries, as indicated by previous studies.[58,59] Therefore, $Li_9Ag_4$ and $Li_4Ag$ may possess excellent electrochemical performance.

**Overall performance evaluation**

In order to select the most suitable solid solution alloy phase and establish the optimal charging and discharging range for achieving optimal performance in practice applications, we conduct a comprehensive analysis of the performance characteristics for various Li-Ag alloys. The theoretical gravimetric capacity[37] of six solid solution phases in the Li-Ag phase diagrams for Ag, LiAg, $Li_9Ag_4$, $Li_4Ag$, $Li_9Ag$, and Li solid solution phases are 207, 63, 214, 409, 797, and 3860 mAh/g, respectively. This refers to the capacities within the $\alpha$ phase, $\beta$ phase, $\gamma_3$ phase, $\gamma_2$ phase, $\gamma_1$ phase, and $\delta$ phase. As the Li concentration increases, the theoretical gravimetric capacity tends to increase. Considering four factors, including chemical stability, Li insertion (Li adsorption, nucleation, and diffusion), mechanical properties, and capacity, for a comprehensive assessment, Figure 4 reveals that $Li_4Ag$ and $Li_9Ag_4$ demonstrate relatively better performance than other phases. Among them, $Li_4Ag$ exhibits the best performance. Therefore, we suggest $Li_4Ag$ is the preferred choice, followed by $Li_9Ag_4$.

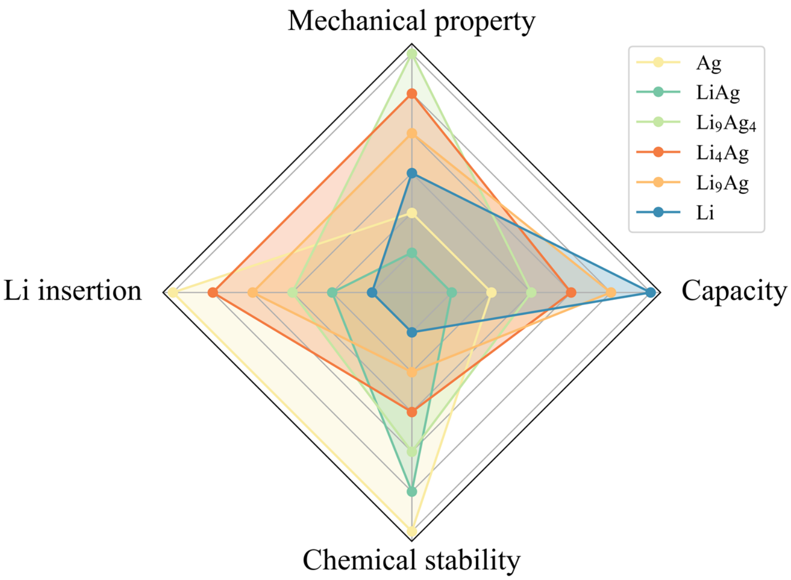

Figure 4. Summary of different Li-Ag alloys performance. $Li_4Ag$ represents the optimal phase, followed by $Li_9Ag_4$.

## Experiment validation.

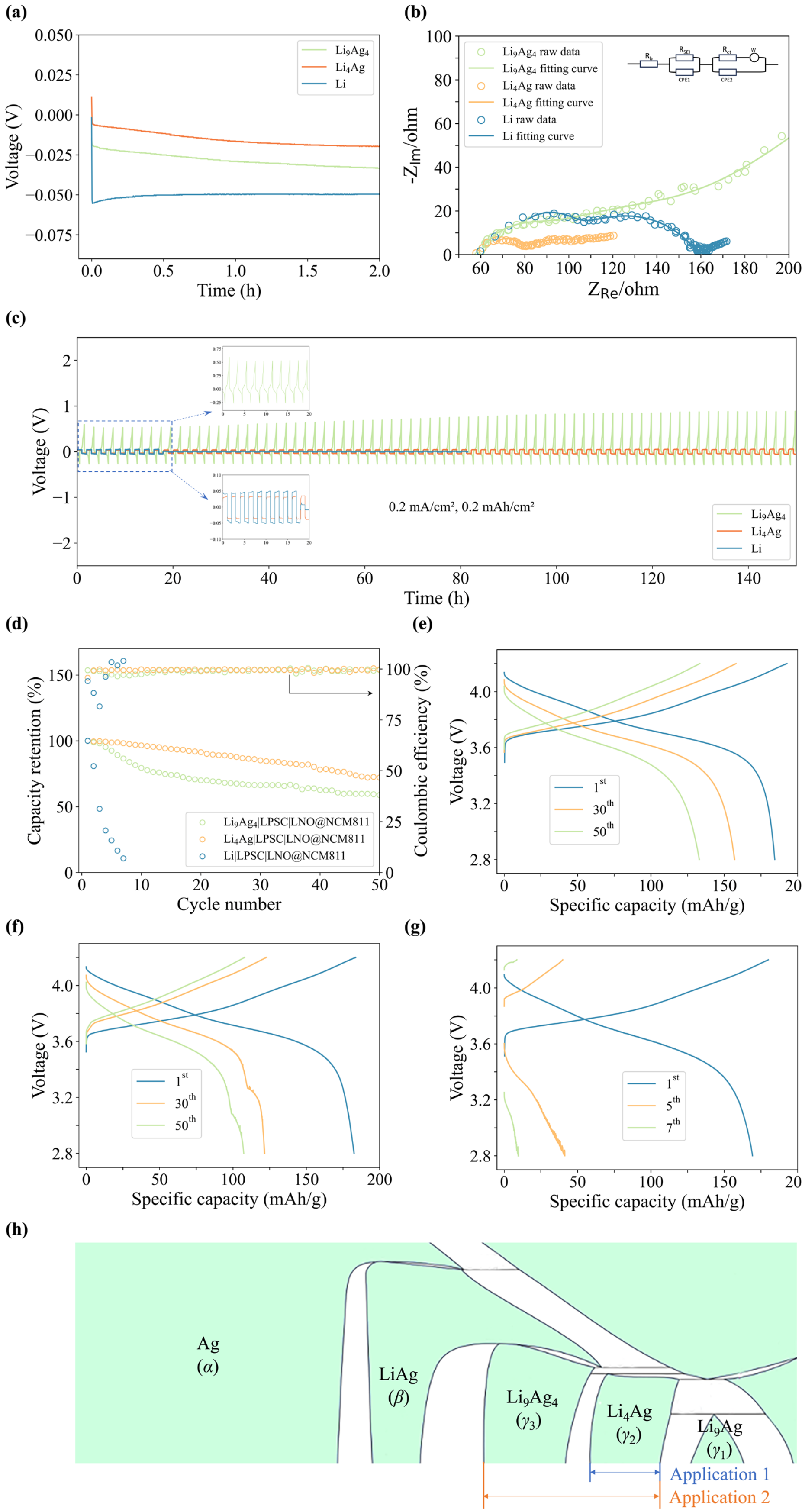
(a)
Voltage (V)
0.050
0.025
0.000
−0.025
−0.050
−0.075
0.0
0.5
1.0
1.5
2.0
Time (h)
$Li_9Ag_4$
$Li_4Ag$
Li
(b)
$-Z_{Im}$/ohm
$Z_{Re}$/ohm
100
80
60
40
20
0
60
80
100
120
140
160
180
200
$Li_9Ag_4$ raw data
$Li_9Ag_4$ fitting curve
$Li_4Ag$ raw data
$Li_4Ag$ fitting curve
Li raw data
Li fitting curve
$R_b$
$R_{SEI}$
$R_{ct}$
W
CPE1
CPE2
(c)
Voltage (V)
2
1
0
−1
−2
0
20
40
60
80
100
120
140
Time (h)
0.2 mA/cm², 0.2 mAh/cm²
$Li_9Ag_4$
$Li_4Ag$
Li
(d)
Capacity retention (%)
Coulombic efficiency (%)
150
100
50
0
100
75
50
25
0
0
10
20
30
40
50
Cycle number
$Li_9Ag_4$|LPSC|LNO@NCM811
$Li_4Ag$|LPSC|LNO@NCM811
Li|LPSC|LNO@NCM811
(e)
Voltage (V)
4.0
3.6
3.2
2.8
0
50
100
150
200
Specific capacity (mAh/g)
1st
30th
50th
(f)
Voltage (V)
4.0
3.6
3.2
2.8
0
50
100
150
200
Specific capacity (mAh/g)
1st
30th
50th
(g)
Voltage (V)
4.0
3.6
3.2
2.8
0
50
100
150
200
Specific capacity (mAh/g)
1st
5th
7th
(h)
Ag
(α)
LiAg
(β)
$Li_9Ag_4$
($\gamma_3$)
$Li_4Ag$
($\gamma_2$)
$Li_9Ag$
($\gamma_1$)
Application 1
Application 2

Figure 5. Electrochemical performance of $Li_9Ag_4$, $Li_4Ag$, and Li anodes. $Li_4Ag$ exhibits smaller nucleation overpotential (η), reduced electrochemical impedance spectroscopy (EIS), stable voltage profiles, and higher capacity retention than $Li_9Ag_4$ and Li. (a) Nucleation overpotential ($\eta$). (b) The Nyquist plots. (c) Voltage behavior of symmetric cells at 0.2 mA/cm$^2$. (d) Cycling performance at 0.25 mA/cm$^2$. Voltage profiles of full cells after various cycles. (e) $Li_4Ag$ |LPSC|LNO@NCM811. (f) $Li_9Ag_4$|LPSC|LNO@NCM811, and (g) Li|LPSC|LNO@NCM811. (h) For the practical application interval, we recommend operating within the $Li_4Ag$ solution phases or from the $Li_9Ag_4$ to the $Li_4Ag$ solution phase.

To validate the DFT calculated results, experiments were conducted on two top-performing phases, $Li_4Ag$ and $Li_9Ag$ (Figure S3), and compared with the Li phase. The SEM images presented in Figure S4a-b and Figure S5a-b illustrate the surfaces of $Li_4Ag$ and $Li_9Ag_4$. Moreover, the surface and cross-section EDS maps (Figure S4c,e and Figure S5c,e) for $Li_4Ag$ and $Li_9Ag_4$ indicate the homogeneous distribution of Ag elements throughout the foil. Furthermore, as depicted in Figure S4d and Figure S5d, both $Li_4Ag$ and $Li_9Ag_4$ exhibit a thickness of approximately 50 μm, suggesting considerable potential for achieving high energy density. The nucleation overpotential ($\eta$) was evaluated as the difference between the initial voltage drop's bottom and the plateau's flat region. As illustrated in Figure 5(a), the $\eta$ values for $Li_4Ag$, $Li_9Ag_4$, and Li were 0, 0, and 6 mV, respectively. The lower nucleation overpotential suggests superior lithiophilicity in $Li_4Ag$ and $Li_9Ag_4$, resulting in uniform nucleation and deposition behavior.

In addition, to evaluate the interfacial resistance of the symmetric cells, including SEI resistance ($R_{SEI}$) and charge transfer resistance ($R_{ct}$), electrochemical impedance spectroscopy (EIS) measurements were utilized. It is well-established that small $R_{SEI}$ leads to enhanced cycling stability, while $R_{ct}$ is associated with redox reactions at the interface. Small $R_{ct}$ indicates faster kinetics in $Li^+$ reduction.[60–62] The Nyquist plots in Figure 5b depict the EIS results for $Li_9Ag_4$, $Li_4Ag$, and Li, with the corresponding fitted $R_{SEI}$ and $R_{ct}$ values in Table S7. Notably, $Li_4Ag$ exhibits the smallest $R_{SEI}$ (12.10 Ω) and $R_{ct}$ (24.33 Ω) compared to $Li_9Ag_4$ ($R_{SEI}$: 25.20 Ω, $R_{ct}$: 43.89 Ω) and Li ($R_{SEI}$: 24.52 Ω,

$R_{\mathrm{ct}}$: 59.79 Ω). The findings suggest that $Li_4Ag$ offers higher cycling stability and faster kinetics in $Li^+$ reduction compared to $Li_9Ag_4$ and Li.

Beyond $\eta$ and EIS tests, the long-term cycling stability was evaluated for $Li_9Ag_4$, $Li_4Ag$, and Li. Symmetric cells were assembled and tested at 0.2 mA/cm$^2$ and 0.2 mAh/cm$^2$. As depicted in Figure 5c, the symmetric cell employing $Li_4Ag$ demonstrates the smallest polarization, showing a remarkable performance advantage over $Li_9Ag_4$ and Li. The large voltage hysteresis observed in the cycling curve of the $Li_9Ag_4$ symmetric cell can be attributed to two main factors: the presence of the LiAg phase with its largest diffusion barrier and the large $R_{\mathrm{SEI}}$ and $R_{\mathrm{ct}}$ for $Li_9Ag_4$.[63] Moreover, both $Li_4Ag$ and $Li_9Ag_4$ maintain stable voltage profiles for 150 hours, while Li's stability is limited to just under 25 hours. This suggests that $Li_9Ag_4$ and $Li_4Ag$ are less prone to dendrites growth than pure Li.

Finally, the full cell tests were conducted to evaluate the practical cycling performance of $Li_9Ag_4$, $Li_4Ag$, and Li. We assembled the full cells, namely, $Li_9Ag_4$|LPSC|LNO@NCM811, $Li_4Ag$|LPSC|LNO@NCM811, and Li|LPSC|LNO@NCM811. The testing involved applying 0.125 mA/cm$^2$ for the first two cycles and 0.25 mA/cm$^2$ for the subsequent cycles, with the mass loading of cathode active material at 7.64 mg/cm$^2$. The results reveal that Li|LPSC|LNO@NCM811 exhibited an inferior cycling lifespan when compared to $Li_9Ag_4$|LPSC|LNO@NCM811 and $Li_4Ag$|LPSC|LNO@NCM811. We conducted tests on Li|LPSC|LNO@NCM811 under high stack pressure. However, during the initial charging, a short circuit was observed (Figure S6). Subsequently, we switched to a lower stack pressure. As illustrated in Figure 5d, after 7 cycles, Li|LPSC|LNO@NCM811's capacity retention is only 10.8%, while after 50 cycles, $Li_9Ag_4$|LPSC|LNO@NCM811 and $Li_4Ag$|LPSC|LNO@NCM811 retained 58.8% and 72.1%, respectively. Therefore, $Li_4Ag$ demonstrates the best cycling performance compared to $Li_9Ag_4$ and Li.

Moreover, in Figures 5e-f, the charge-discharge profiles for $Li_9Ag_4$|LPSC|LNO@NCM811 and $Li_4Ag$|LPSC|LNO@NCM811 during the 1st, 30th, and 50th cycles are presented. The $Li_9Ag_4$|LPSC|LNO@NCM811 full cell exhibits areal capacities of 183, 121, and 107 mAh/g in the 1st, 30th, and 50th cycles, respectively. In comparison, the $Li_4Ag$|LPSC|LNO@NCM811 demonstrates areal capacities of 184, 157, and 133 mAh/g for the corresponding cycles. Notably, Li|LPSC|LNO@NCM811 shows lower discharge specific capacities than the aforementioned cells (Figure 5g). Crucially, the $Li_4Ag$|LPSC|LNO@NCM811 full cell displays highly reversible charging and discharging capacities, along with lower voltage degradation when compared to both $Li_9Ag_4$|LPSC|LNO@NCM811 and Li|LPSC|LNO@NCM811.

Based on the DFT calculations and experimental results mentioned above, we have identified that $Li_4Ag$ is the most promising phase, followed by $Li_9Ag_4$. The critical question is how to effectively utilize Li-Ag alloys in practical applications. As illustrated in Figure 5h, we recommend two practical application intervals. Firstly, we suggest operating within the $Li_4Ag$ solution phases, which can provide a capacity of 409mAh/g. Secondly, we recommend working within the interval from the $Li_9Ag_4$ solution phase to the $Li_4Ag$ solution phase, which offers a capacity of 696 mAh/g. Both capacities are higher than graphite (372 mAh/g).[64] By striking a balance between performance and energy density, this recommended interval demonstrates significant potential for practical applications.

## Conclusion

Our study combined DFT calculations with experiments to compare Li-Ag alloys with pure Li in ASSLBs. Firstly, Li-Ag alloys exhibited smaller $\Delta G_{\mathrm{nucle}}$ compared to pure Li, as confirmed both computationally and experimentally. Additionally, $Li_4Ag$ emerged as the top-performing alloy in terms of Li insertion, mechanical properties, chemical stability, and capacity. For instance, at the current density and areal capacity of 0.2 mA/cm$^2$ and 0.2 mAh/cm$^2$, our symmetric cell operated for approximately 150 hours without overpotential decay. We also achieved 72.1% capacity retention after 50 cycles under an area loading of 7.64 mg/cm$^2$ and a current density of 0.25 mA/cm$^2$. Finally, we suggested cycling within the $Li_4Ag$ solution phases or from the $Li_9Ag_4$ solution phase to the $Li_4Ag$ solution phase. This work provides insights to optimize alloy compositions and practical application intervals, unlocking the full potential of Li-Ag alloys for future battery applications.

## Acknowledgments

This work was supported by the National Natural Science Foundation of China (No. 52072240 and 22222204) and the Materials Genome Initiative Center at Shanghai Jiao Tong University. All simulations were carried out using computational resources from the Center for High Performance Computing at Shanghai Jiao Tong University.

## References

1. Wang, Z. *et al.* Soft Carbon-Thiourea with Fast Bulk Diffusion Kinetics for Solid-State Lithium Metal Batteries. *Advanced Materials* **36**, 2310395 (2024).
2. Niu, C. *et al.* High-energy lithium metal pouch cells with limited anode swelling and long stable cycles. *Nat Energy* **4**, 551–559 (2019).
3. Zhang, X.-Q. *et al.* A Sustainable Solid Electrolyte Interphase for High-Energy-Density Lithium Metal Batteries Under Practical Conditions. *Angewandte Chemie International Edition* **59**, 3252–3257 (2020).
4. Li, S. *et al.* Synergistic Dual-Additive Electrolyte Enables Practical Lithium-Metal Batteries. *Angewandte Chemie International Edition* **59**, 14935–14941 (2020).
5. Ma, T. *et al.* High-areal-capacity and long-cycle-life all-solid-state battery enabled by freeze drying technology. *Energy Environ. Sci.* **16**, 2142–2152 (2023).
6. Jin, S. *et al.* High Areal Capacity and Lithium Utilization in Anodes Made of Covalently Connected Graphite Microtubes. *Advanced Materials* **29**, 1700783 (2017).
7. Yang, Y. *et al.* Stable lithium metal anode enabled by in situ formation of a Li 3 N/Li–Bi alloy hybrid layer. *Chemical Communications* **59**, 936–939 (2023).
8. Liu, Y. *et al.* Lithiophilic sites dependency of lithium deposition in Li metal host anodes. *Nano Energy* **94**, 106883 (2022).
9. Li, R. *et al.* Air-Stable Protective Layers for Lithium Anode Achieving Safe Lithium Metal Batteries. *Small Methods* **7**, 2201177 (2023).
10. Xu, R. *et al.* Artificial Interphases for Highly Stable Lithium Metal Anode. *Matter* **1**, 317–344 (2019).
11. Camacho-Forero, L. E., Smith, T. W., Bertolini, S. & Balbuena, P. B. Reactivity at the Lithium–Metal Anode Surface of Lithium–Sulfur Batteries. *J. Phys. Chem. C* **119**, 26828–26839 (2015).
12. Aurbach, D., Zinigrad, E., Cohen, Y. & Teller, H. A short review of failure mechanisms of lithium metal and lithiated graphite anodes in liquid electrolyte solutions. *Solid state ionics* **148**, 405–416 (2002).
13. Lin, L. *et al.* A Better Choice to Achieve High Volumetric Energy Density: Anode-Free Lithium-Metal Batteries. *Advanced Materials* **34**, 2110323 (2022).
14. Riley, L. A. *et al.* Conformal Surface Coatings to Enable High Volume Expansion Li-Ion Anode Materials. *ChemPhysChem* **11**, 2124–2130 (2010).

15. Liu, Y. *et al.* Integrated Gradient Cu Current Collector Enables Bottom-Up Li Growth for Li Metal Anodes: Role of Interfacial Structure. *Advanced Science* 2301288 (2023).
16. Zhao, B. *et al.* Uniform Li Deposition Sites Provided by Atomic Layer Deposition for the Dendrite-free Lithium Metal Anode. *ACS Appl. Mater. Interfaces* **12**, 19530–19538 (2020).
17. Xiao, J. How lithium dendrites form in liquid batteries. *Science* **366**, 426–427 (2019).
18. Li, L. *et al.* Self-heating–induced healing of lithium dendrites. *Science* **359**, 1513–1516 (2018).
19. Zhang, S. *et al.* Tackling realistic Li+ flux for high-energy lithium metal batteries. *Nat Commun* **13**, 5431 (2022).
20. Jana, A. & García, R. E. Lithium dendrite growth mechanisms in liquid electrolytes. *Nano Energy* **41**, 552–565 (2017).
21. Song, H. *et al.* Dendrite-Free Composite Li Anode Assisted by Ag Nanoparticles in a Wood-Derived Carbon Frame. *ACS Appl. Mater. Interfaces* **11**, 18361–18367 (2019).
22. Zuo, Z. *et al.* Lithiophilic Silver Coating on Lithium Metal Surface for Inhibiting Lithium Dendrites. *Frontiers in Chemistry* **8**, (2020).
23. Ye, Y. *et al.* Solid-Solution or Intermetallic Compounds: Phase Dependence of the Li-Alloying Reactions for Li-Metal Batteries. *J. Am. Chem. Soc.* **145**, 24775–24784 (2023).
24. Zhang, C. *et al.* Non-sticky Li-alloy leaves for long-lasting secondary batteries. *Energy Environ. Sci.* **15**, 5251–5260 (2022).
25. Li, B. *et al.* Dual Protection of a Li–Ag Alloy Anode for All-Solid-State Lithium Metal Batteries with the Argyrodite $Li_6PS_5Cl$ Solid Electrolyte. *ACS Appl. Mater. Interfaces* **14**, 37738–37746 (2022).
26. He, X. *et al.* The passivity of lithium electrodes in liquid electrolytes for secondary batteries. *Nat Rev Mater* **6**, 1036–1052 (2021).
27. Famprikis, T., Canepa, P., Dawson, J. A., Islam, M. S. & Masquelier, C. Fundamentals of inorganic solid-state electrolytes for batteries. *Nat. Mater.* **18**, 1278–1291 (2019).
28. Xu, C., Ahmad, Z., Aryanfar, A., Viswanathan, V. & Greer, J. R. Enhanced strength and temperature dependence of mechanical properties of Li at small scales and its implications for Li metal anodes. *Proc. Natl. Acad. Sci. U.S.A.* **114**, 57–61 (2017).
29. Sun, J. *et al.* Lithium deposition mechanism on Si and Cu substrates in the carbonate electrolyte. *Energy Environ. Sci.* **15**, 5284–5299 (2022).
30. He, Y. *et al.* Regulation of Dendrite-Free Li Plating via Lithiophilic Sites on Lithium-Alloy Surface. *ACS Appl. Mater. Interfaces* **14**, 33952–33959 (2022).
31. Blöchl, P. E. Projector augmented-wave method. *Phys. Rev. B* **50**, 17953–17979 (1994).
32. Hafner, J. Ab-initio simulations of materials using VASP: Density-functional theory and beyond. *Journal of Computational Chemistry* **29**, 2044–2078 (2008).

33. Perdew, J. P., Burke, K. & Ernzerhof, M. Generalized Gradient Approximation Made Simple. *Phys. Rev. Lett.* **77**, 3865–3868 (1996).
34. He, Y. *et al.* Discovery of an Unexpected Metal Dissolution of Thin-Coated Cathode Particles and Its Theoretical Explanation. *Advanced Theory and Simulations* **3**, 2000002 (2020).
35. Xu, Z.-M., Bo, S.-H. & Zhu, H. $LiCrS_2$ and $LiMnS_2$ Cathodes with Extraordinary Mixed Electron–Ion Conductivities and Favorable Interfacial Compatibilities with Sulfide Electrolyte. *ACS Appl. Mater. Interfaces* **10**, 36941–36953 (2018).
36. Taillades, G. & Sarradin, J. Silver: high performance anode for thin film lithium ion batteries. *Journal of Power Sources* **125**, 199–205 (2004).
37. Jin, S. *et al.* Solid–Solution-Based Metal Alloy Phase for Highly Reversible Lithium Metal Anode. *J. Am. Chem. Soc.* **142**, 8818–8826 (2020).
38. Park, C.-M., Jung, H. & Sohn, H.-J. Electrochemical Behaviors and Reaction Mechanism of Nanosilver with Lithium. *Electrochem. Solid-State Lett.* **12**, A171 (2009).
39. Obrovac, M. N. & Chevrier, V. L. Alloy Negative Electrodes for Li-Ion Batteries. *Chem. Rev.* **114**, 11444–11502 (2014).
40. Yan, W. *et al.* Hard-carbon-stabilized Li–Si anodes for high-performance all-solid-state Li-ion batteries. *Nat Energy* **8**, 800–813 (2023).
41. Heligman, B. T. & Manthiram, A. Elemental Foil Anodes for Lithium-Ion Batteries. *ACS Energy Lett.* **6**, 2666–2672 (2021).
42. Lewis, J. A., Cavallaro, K. A., Liu, Y. & McDowell, M. T. The promise of alloy anodes for solid-state batteries. *Joule* **6**, 1418–1430 (2022).
43. Manthiram, A., Yu, X. & Wang, S. Lithium battery chemistries enabled by solid-state electrolytes. *Nat Rev Mater* **2**, 1–16 (2017).
44. Ha, S. *et al.* Lithiophilic MXene-Guided Lithium Metal Nucleation and Growth Behavior. *Adv Funct Materials* **31**, 2101261 (2021).
45. Euchner, H. & Groß, A. Atomistic modeling of Li- and post-Li-ion batteries. *Phys. Rev. Materials* **6**, 040302 (2022).
46. Choi, S. H. *et al.* Marginal Magnesium Doping for High-Performance Lithium Metal Batteries. *Adv. Energy Mater.* **9**, 1902278 (2019).
47. Wang, D. *et al.* Towards High-Safe Lithium Metal Anodes: Suppressing Lithium Dendrites via Tuning Surface Energy. *Adv. Sci.* **4**, 1600168 (2017).
48. Kamrani Moghaddam, L., Ramezani Paschepari, S., Zaimy, M. A., Abdalaian, A. & Jebali, A. Data Descriptor: Surface energies of elemental crystals. *Cancer Gene Ther* **23**, 321–325 (2016).
49. Liu, T. *et al.* Lithiophilic Ag/Li composite anodes *via* a spontaneous reaction for Li nucleation with a reduced barrier. *J. Mater. Chem. A* **7**, 20911–20918 (2019).
50. Lee, S. *et al.* Design of a lithiophilic and electron-blocking interlayer for dendrite-free lithium-metal solid-state batteries. *Science Advances* **8**, eabq0153 (2022).
51. Zhang, P. *et al.* A first principles study of the mechanical properties of Li–Sn alloys. *RSC Adv.* **5**, 36022–36029 (2015).

---

52. Pavlic, O. *et al.* Design of Mg alloys: The effects of Li concentration on the structure and elastic properties in the Mg-Li binary system by first principles calculations. *Journal of Alloys and Compounds* **691**, 15–25 (2017).
53. Du, F. *et al.* Thermally insulating and fire-retardant bio-mimic structural composites with a negative Poisson's ratio for battery protection. *Carbon Energy* **5**, e353 (2023).
54. Pugh, S. F. XCII. Relations between the elastic moduli and the plastic properties of polycrystalline pure metals. *The London, Edinburgh, and Dublin Philosophical Magazine and Journal of Science* **45**, 823–843 (1954).
55. Vitos, L., Korzhavyi, P. A. & Johansson, B. Elastic Property Maps of Austenitic Stainless Steels. *Phys. Rev. Lett.* **88**, 155501 (2002).
56. Mouhat, F. & Coudert, F.-X. Necessary and sufficient elastic stability conditions in various crystal systems. *Phys. Rev. B* **90**, 224104 (2014).
57. Turley, J. & Sines, G. The anisotropy of Young's modulus, shear modulus and Poisson's ratio in cubic materials. *J. Phys. D: Appl. Phys.* **4**, 264 (1971).
58. Sandu, G. *et al.* Surface Coating Mediated Swelling and Fracture of Silicon Nanowires during Lithiation. *ACS Nano* **8**, 9427–9436 (2014).
59. Choi, Y.-S., Park, J.-H., Ahn, J.-P. & Lee, J.-C. Anisotropic Swelling Governed by Orientation-Dependent Interfacial Na Diffusion in Single-Crystalline Sb. *Chem. Mater.* **31**, 1696–1703 (2019).
60. Ranganathan Gaddam, R., Katzenmeier, L., Lamprecht, X. & S. Bandarenka, A. Review on physical impedance models in modern battery research. *Physical Chemistry Chemical Physics* **23**, 12926–12944 (2021).
61. Li, X., Yang, G., Zhang, S., Wang, Z. & Chen, L. Improved lithium deposition on silver plated carbon fiber paper. *Nano Energy* **66**, 104144 (2019).
62. Zhang, S. S., Xu, K. & Jow, T. R. EIS study on the formation of solid electrolyte interface in Li-ion battery. *Electrochimica Acta* **51**, 1636–1640 (2006).
63. Wang, Z. *et al.* Tailoring lithium concentration in alloy anodes for long cycling and high areal capacity in sulfide-based all solid-state batteries. *eScience* **3**, 100087 (2023).
64. Hao, Z. *et al.* Anion-derived solid electrolyte interphase realized in usual-concentration electrolyte for Li metal batteries. *Nano Res.* **16**, 12647–12654 (2023).